Nanoscale

ROYAL SOCIETY OF CHEMISTRY

PAPER

View Article Online
View Journal | View Issue

Cite this: *Nanoscale*, 2023, **15**, 11875

Dual functionality of ferrocene-based metallopolymers as radical scavengers and nanoparticle stabilizing agents†

Nizar B. Alsharif,[a] Tibor Gergo Halmágyi,[b] Mark A. Hempenius,[c] G. Julius Vancso,[c] Corinne Nardin[b] and Istvan Szilagyi *[a]

The beneficial redox properties of ferrocene-based polymers have been utilized during *in situ* preparation of metallic nanoparticles, while such redox features also indicate a great promise in applications as free radical scavengers. Here, colloidal dispersions of an antioxidant nanozyme composed of amidine-functionalized polystyrene latex (AL) nanoparticles, negatively charged poly(ferrocenylsilane) (PFS(–)) organometallic polyions, and ascorbic acid (AA) were formulated. The AL was first functionalized with PFS(–). Increasing the polymer dose resulted in charge neutralization and subsequent charge reversal of the particles. The strength of repulsive interparticle forces of electrostatic nature was significant at low and high doses leading to stable colloids, while attractive forces dominated near the charge neutralization point giving rise to unstable dispersions. The saturated PFS(–) layer adsorbed on the surface of the AL (p-AL nanozyme) enhanced the colloidal stability against salt-induced aggregation without affecting the pH-dependent charge and size of the particles. The joint effect of PFS(–) and the AA in radical decomposition was observed indicating the antioxidant potential of the system. The immobilization of PFS(–) deteriorated its scavenging activity, yet the combination with AA improved this feature. The results indicate that p-AL-AA is a promising radical scavenger since the high colloidal stability of the particles allows application in heterogeneous systems, such as in industrial manufacturing processes, where antioxidants are required to maintain acceptable product quality.

Received 4th May 2023,
Accepted 10th June 2023

DOI: 10.1039/d3nr02063k

rsc.li/nanoscale

1. Introduction

Poly(ferrocenylsilane)s (PFSs) have proved to be a suitable material for the preparation of metallic nanoparticles due to their redox-sensitive nature, which is attributed to the ferrocene group present in the main chain that can be oxidized to ferrocenium.[1,2] The obtained PFS–nanoparticle systems often possess excellent redox sensitivity and reversible redox kinetics, while a color change response that accompanies the redox process enables the use of the PFS-functionalized metallic nanoparticles as building blocks in colorimetric detection.[3] Besides, the redox properties stimulated researchers to design PFS films on planar silicon, gold, or glassy carbon surfaces to develop electrochemical sensors exhibiting high sensitivity and stable responses to target molecules such as ascorbic acid (AA).[4,5] Apart from the above-mentioned advantageous redox features utilized in sensing, there are two additional important potential uses of PFS, which are worthy of further exploration. These include their effect on the colloidal stability of particle dispersions and possible radical scavenging activity.

On the one hand, it was proved that PFS can serve as a stabilizer for gold particles.[3] Since PFS can be considered as a polymer of significant line charge density (*i.e.*, a so-called polyelectrolyte), the explanation of the origin of surface forces induced by PFS adsorption seems straightforward. Accordingly, electrostatic repulsive forces between PFS-coated charged surfaces are predicted by the classical theory of Derjaguin, Landau, Verwey, and Overbeek (DLVO),[6–8] in terms of the repulsion by the overlapping electrical double layers. This theory also assumes the constant presence of attractive van der Waals forces, while non-DLVO attraction may occur *via* patch-charge[9,10] or bridging interactions.[11,12] In addition, partially adsorbed polymer chains dangling into the solution from the surface may establish steric repulsion between approaching particles.[13–15] Such interparticle forces were reported in various particle–polyelectrolyte systems in the past

[a]*MTA-SZTE Lendület Biocolloids Research Group, Department of Physical Chemistry and Materials Science, Interdisciplinary Research Center, University of Szeged, H-6720 Szeged, Hungary. E-mail: szistvan@chem.u-szeged.hu*
[b]*Université de Pau et des Pays de l'Adour, E2S UPPA, CNRS, IPREM, F-64053 Pau, France*
[c]*Sustainable Polymer Chemistry, University of Twente, NL-7522NB Enschede, the Netherlands*

† Electronic supplementary information (ESI) available. See DOI: https://doi.org/10.1039/d3nr02063k

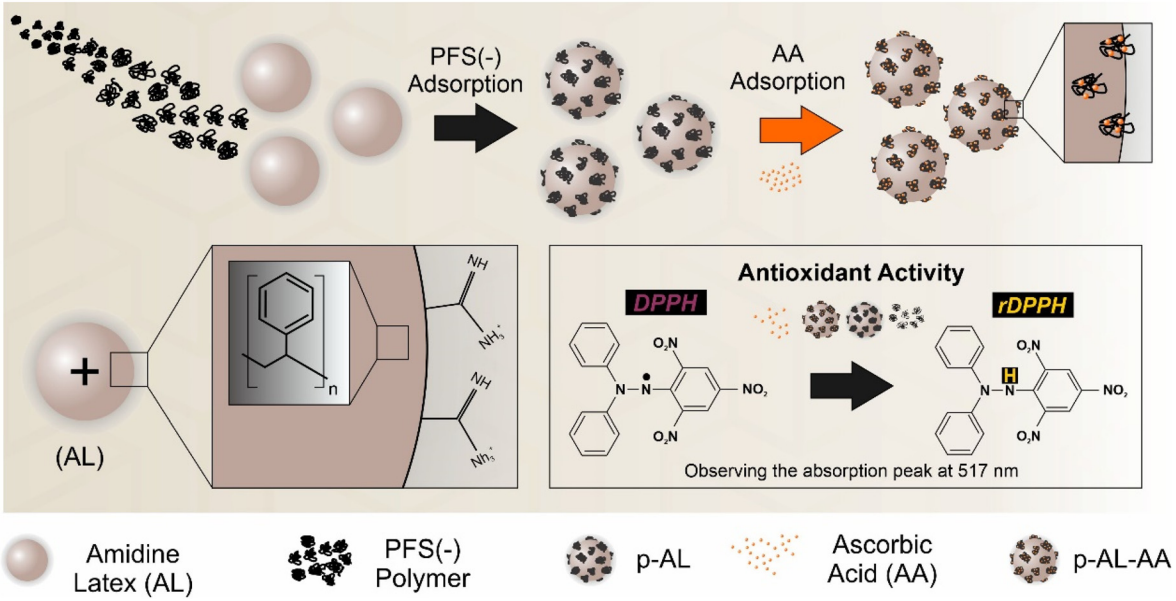

Scheme 1 Illustration of the adsorption of PFS(−) and ascorbic acid on AL to obtain antioxidant nanozymes, together with a sketch of the AL nanobead structure. The main principle of the radical scavenging activity assessment is also given.

few decades.[16–20] Beyond some pioneering works with gold–PFS composites,[2,3] the effect of PFS adsorption on the colloidal stability of dispersed nanoparticles has not been investigated.

On the other hand, polymer-based free radical scavenger nanoparticles, *i.e.*, nanozymes, are widely applied as antioxidants in various fields,[21–25] and this can be a potential application for PFS-containing nanoparticulate systems, too. Although ferrocene itself was used to inhibit the low-temperature oxidation chemistry in fuel processing technologies,[26] while ferrocene-containing peptide conjugates were developed as potential antioxidant enzyme mimics,[27] the antioxidant potential of polymeric PFS has not been assessed. However, the studies mentioned indicate great promise for the application of PFS derivatives as free radical scavengers.

In order to tackle the above-mentioned scavenging possibility, the present study focuses on the role of PFS as a stabilizer of nanoparticles and as an antioxidant in nanozyme systems. The interfacial features of negatively charged PFS (denoted as PFS(−)) possessing sulfonate and carboxylate groups were probed by examining its ability to adsorb and modify the surface properties of amidine-functionalized latex nanobeads (AL) and its influence on the aggregation of the particles. In addition, its antioxidant potential along with AA was evaluated *via* a standard radical scavenging assay. These steps are illustrated in Scheme 1.

The effect of the pH, ionic strength, and the dose of PFS(−) was systematically investigated. The colloidal properties of the polymer-based nanozymes were expected to affect the redox activity of PFS(−); therefore, the redox-sensitive feature was studied by testing its radical scavenging potential alone, immobilized on the AL and in the presence of AA.

2. Experimental

2.1. Materials

Amidine-functionalized polystyrene latex beads (mean diameter by transmission electron microscopy (TEM): 0.068 μm, coefficient of variation in diameter: 12.5%, solid concentration: 4% w/v in dispersion, density: 1.055 g mL^{-1} and surface charge density: 4.8 μC cm^{-2}) were purchased from Fischer Scientific (USA). Methanol (AnalaR NORMAPUR), NaOH (AnalaR NORMAPUR, ≥99.3%), HCl (AnalaR NORMAPUR, 37 w/w%), ascorbic acid (AA), and NaCl (99.9%) were purchased from VWR™ (Hungary). The 2,2-diphenyl-1-picrylhydrazyl (DPPH) radical (95%) was obtained from Alfa Aesar (USA). The Hellmanex® III cleaning agent was purchased from Hellma (Germany). Polyvinyl difluoride (PVDF)-based 0.1 μm syringe filters (MILLEX-VV, Germany) were used to filter ultrapure water obtained from a VWR™ Puranity TU 3 UV/UF + system.

During the synthesis of the $(Et_4N)_2SO_3$ reagent, 0.215 mL Me_2SO_3 (2.53 mmol) and 2.1 mL Et_4NOH (35 w/w in water, 5.0 mmol) were mixed in 2 mL DMSO at room temperature for 4 hours. Slight precipitation of the product was observed during this time. The residual solvents were then evaporated from DMSO, and the material was used as is in the synthesis of water-soluble anionic PFS(−) polymers.

2.2. Preparation of carboxyl-functionalized poly (ferrocenylsilane)

Carboxyl-functionalized PFS(−) was prepared by a multi-step procedure (1–5) as shown in Scheme 2, as detailed below.

(2) *PFS-I*: A solution of PFS-Cl (compound **1** in Scheme 2, 241.8 mg; 0.793 mmol repeat units), KI (120.0 mg; 0.724 mmol), dicyclohexano-18-crown-6 (78.4 mg; 0.210 mmol), and iodopro-

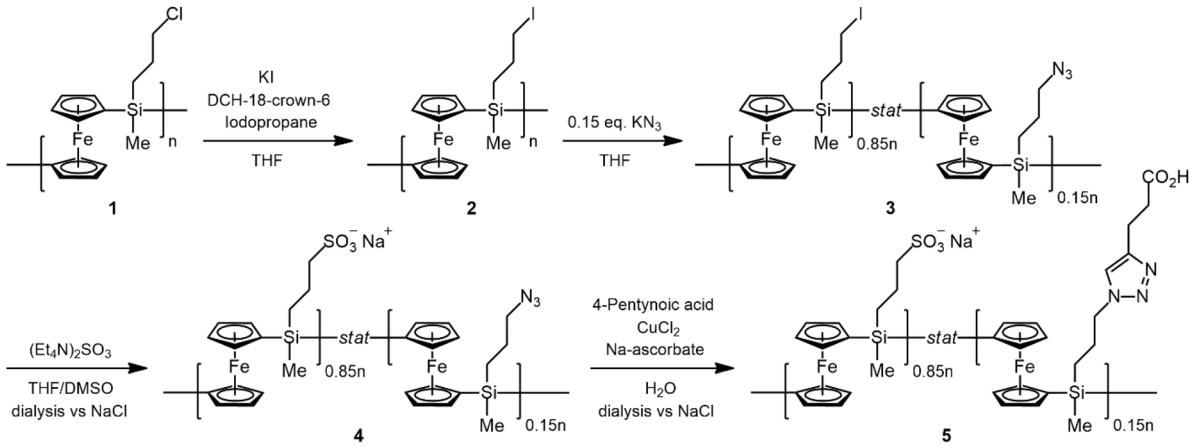

Scheme 2 Schematic illustration of the preparation route of PFS(−). Details of steps (2), (3), (4), and (5) are described in the text.

pane (2 mL; 19.6 mmol) in THF was stirred at 45 °C for a week. The polymer was precipitated in MeOH, dried, and stirred with the same reagents at 45 °C until the completion of the halogen exchange. The polymer was then precipitated and washed in MeOH and dried. Successful iodide substitution was confirmed by ^{1}H NMR in benzene-d6 (see Fig. S1 in the ESI†).

(3) *PFS-I/N$_3$* (15%): PFS-I (244.7 mg; 0.618 mmol repeat units) was dissolved in 10 mL THF, and then KN_3 (2.5 mg; 0.031 mmol) dissolved in 5 mL DMSO was added. The reaction was left to proceed at 45 °C overnight. The resulting polymer was then precipitated and washed in MeOH followed by drying. Successful azide substitution was confirmed by ^{1}H NMR in benzene-d6 (Fig. S2†) and D_2O (Fig. S3†).

(4) *PFS(−)/N$_3$* (15%): PFS-I/N_3 (15%; 96.2 mg; 0.251 mmol) was dissolved in 20 mL THF, and then 2 mL DMSO containing $(Et_4N)SO_3$ and an additional 2 mL DMSO solvent were added to set the solvent ratio of THF : DMSO to 5 : 1. The reaction was left to proceed at 35 °C over 3 days. At the endpoint, the product, now insoluble in THF, was concentrated in the DMSO phase. Thereafter, the mixture was transferred to a dialysis hose (benzoylated cellulose, cut-off: 14 kDa) and dialyzed against ultrapure water, then 3 times against 0.1 M NaCl solution, and then against water again. The resulting solution was directly used in the subsequent step.

(5) *PFS(−)/COOH* (15%): PFS(−)/N_3 (15%; 118.9 mg; 0.310 mmol repeating units) was dissolved in water, and 4-pentynoic acid (152.7 mg; 1.56 mmol), $CuCl_2$ (30 mg; 0.223 mmol) and sodium ascorbate (64.0 mg; 0.363 mmol) were added. The reaction was left to proceed at 35 °C. The resulting mixture was dialyzed against ultrapure water, then 3 times against 0.1 M NaCl solution, and then against water again. The solvent was evaporated, and the polymer was finally dried under vacuum.

2.3. Light scattering

Zeta potential and hydrodynamic radius (R_h) values were determined in light scattering measurements to assess the colloidal stability of the particle dispersions at (25.0 ± 0.2) °C. The zeta potential was measured by electrophoretic light scattering using a Litesizer™ 500 (Anton Paar, Austria) device (a 40 mW semiconductor laser diode operating at a 658 nm wavelength and 200 V voltage was applied). First, the electrophoretic mobility values were recorded and converted to zeta potentials using the Smoluchowski equation.[28] The 2.0 mL samples were left to equilibrate for 2 hours at room temperature prior to the measurements, which were executed in omega-shaped plastic cuvettes (Anton Paar). The zeta potential values were reported as an average of 5–8 runs with approximately ±5 mV accuracy.

The pH-dependent surface charging of the bare and functionalized AL was probed by measuring the zeta potentials at a constant ionic strength (1 mM) throughout the pH range of 3–11. In these experiments, 25 mg L^{-1} acidic (pH 3) and alkaline (pH 11) dispersions of the relevant materials were prepared. Then, by mixing various volumes of the two stocks, a series of secondary dispersions, the pH of which gradually changed from 3 to 11, were obtained. This procedure helped to maintain constant ionic strength and material concentration, while altering the pH in the range of interest. Besides, the same particle concentration was used in all other light scattering measurements, in which pH 4.0 was set in the samples.

The hydrodynamic radius values of the particles were determined by dynamic light scattering (DLS) using an ALV-NIBS/HPPS (Germany) particle sizer equipped with a 2.5 mW HeNe (632.8 nm wavelength) laser source. The intensity of the light was collected at a scattering angle of 173°. The cumulant fit was applied to analyze the autocorrelation function and to obtain the decay rate constants, which were converted to translational diffusion coefficient values to calculate the hydrodynamic radii with the Stokes–Einstein equation.[29,30]

In time-resolved DLS, the determination of apparent aggregation rate constants (k_{app}) was possible using the following equation:[31]

$$k_{app} = \frac{1}{R_h(0)} \cdot \left(\frac{dR_h(t)}{dt}\right)_{t\to 0} \quad (1)$$

where $R_h(0)$ is the hydrodynamic radius of non-aggregated monomer particles and $\frac{dR_h(t)}{dt}$ is the rate of change of the

hydrodynamic radii, *i.e.*, the slope of the radii-time plots. This protocol enables investigation of the early stages of particle aggregation, while it is not suitable for following the cluster formation of aggregated particles. The stability ratio (W) provides a measure of colloidal stability and can be obtained as:[32]

$$W = \frac{k_{\mathrm{app(fast)}}}{k_{\mathrm{app}}} \quad (2)$$

where $k_{\mathrm{app(fast)}}$ is the apparent aggregation rate constant in rapidly aggregating samples, *e.g.*, at 1.0 M ionic strength, at which attractive interactions are dominant and electrostatic forces are screened. Note that the stability ratio is directly proportional to the stability of a colloidal dispersion. Measurements in highly stable dispersions yield high or not even measurable stability ratio values, whereas they are close to unity in unstable samples. The time-resolved DLS measurements were initiated immediately upon the addition of the desired volume of the aggregating agents, NaCl or PFS(−). The stability ratio data are subject to about 10% measurement error.

2.4. The DPPH scavenging activity

The radical decomposing potential of the materials, which is an indication of the antioxidant capacity, was assessed with the DPPH assay.[33,34] The DPPH radical shows a dark purple color with a broad absorption band around 517 nm. A potential radical scavenger or antioxidant compound converts DPPH into a yellow product, resulting in decreased absorption at 517 nm, which can be quantitatively followed by UV-vis spectrophotometry. In a typical measurement, various volumes of the material in question were added to a methanol solution containing a fixed amount of DPPH. Hence, highly concentrated stocks were used to minimize the volume of the aqueous phase in the final sample. The change in the absorbance was monitored for 10 minutes in polystyrene cuvettes (VWR, 10 mm light path length) using a Thermo Scientific Genesys S10 (USA) spectrophotometer. The percentage of remaining DPPH (DPPH%) after termination of the reaction was calculated as follows:[35]

$$\mathrm{DPPH\%} = \frac{A}{A_0} \times 100\% \quad (3)$$

where A is the absorbance measured 10 minutes after the reaction starts, while A_0 is the initial absorbance. The concentration necessary to reach a 50% reduction of DPPH is the effective concentration (EC_{50}), which is commonly reported in such assays. The precision of such measurements was about 5%.

3. Results and discussion

3.1. Colloidal characterization of the AL

The pH-dependent zeta potential and hydrodynamic radius data of the AL were determined using electrophoresis and DLS, respectively (Fig. 1a). Accordingly, the AL forms highly stable dispersions in acidic, neutral, and alkaline pH regimes, as evidenced by the nearly constant hydrodynamic radius values of 36.6 ± 0.3 nm. This value is in good agreement with the TEM radius (34 nm) reported by the manufacturer in the dry state. Note that such a deviation between DLS and TEM sizes is due to the measure of the hydrodynamic sphere and the presence of trace aggregates in colloidal form, resulting in a larger DLS size. The zeta potential data, however, show that AL undergoes surface charge reduction as the pH is increased. In more acidic media, amidine groups are progressively protonated resulting in a highly positive charge. Nevertheless, as the

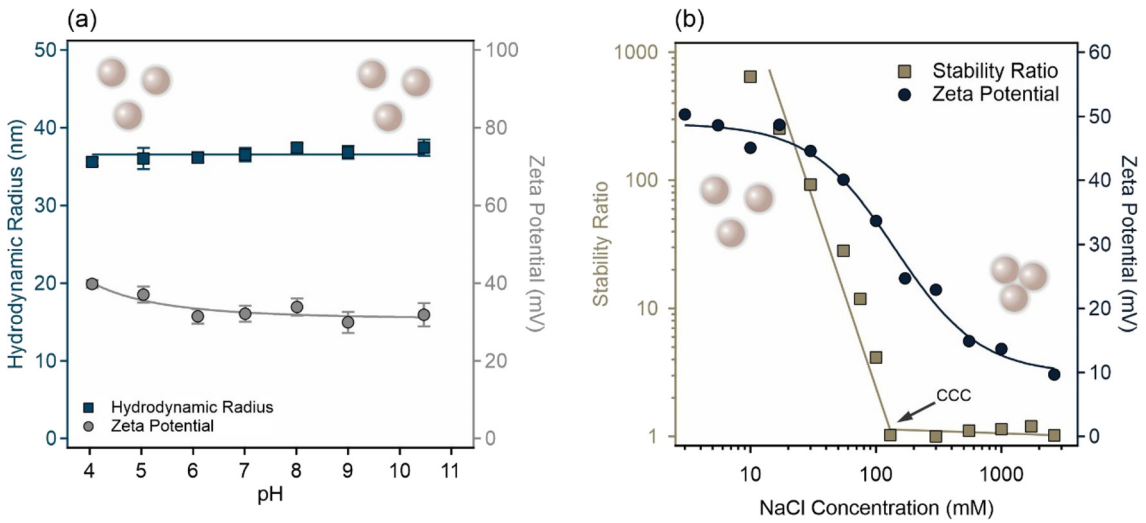

Fig. 1 Characterization of colloidal AL. (a) Hydrodynamic radius and zeta potential of AL as a function of the pH. The ionic strength and AL concentration were maintained at 1.0 mM and 25 mg L^{-1}, respectively. The solid line for the zeta potential serves to guide the eye, while in the case of hydrodynamic radius, it corresponds to a linear fit to determine the average radius value. (b) Stability ratio and zeta potential values of AL at different NaCl concentrations at pH 4.0. The lines are traced for eye-guidance purposes only. The inset graphics illustrate stable and aggregating particles.

pH becomes more alkaline, these surface amidine groups gradually deprotonate leading to a reduction in the surface charge. Although significant deprotonation may have occurred at the alkaline extreme point, *i.e.*, pH 11, AL still maintained significant surface charge to prevent aggregation. Thus, the colloidal stability of AL aqueous dispersions was attributed to strong electrostatic repulsive forces. Similar trends were typically observed for such functionalized latex particles, where the high surface charge gives rise to robust stability.[36–40]

Time-resolved DLS has proved to be a suitable technique to determine the aggregation rate of colloidal and nanoparticles in dispersions.[31] Its main advantage over other techniques[41] such as rheology and turbidity measurements is that it allows the investigation of early stages of particle aggregation and thus the origin of the interparticle forces can be identified. The salt tolerance of AL dispersions was assessed in the ionic strength range from 1 to 3000 mM, adjusted using NaCl. As shown in Fig. 1b, increasing the NaCl concentration leads to a gradual decrease in the stability ratios indicating higher rates of particle aggregation, and hence, severe destabilization of the dispersions. At low salt levels, the dispersions exhibited a high stability ratio, resulting in slow particle aggregation and stable systems. The trend in the zeta potential was also reflected in the stability ratio data. In the low salt concentration regime, the high zeta potential gave rise to strong electrostatic repulsive forces and high (or not even measurable) stability ratios, whereas at a high salt level, the low zeta potential resulted in heavy aggregation indicated by stability ratio values close to unity.

In terms of the DLVO theory,[6,36,37] the addition of salts leads to a reduction in the Debye length and screening of the surface charge followed by weakening of the repulsive electrostatic forces developed by overlapping electrical double layers. This condition leads to rapid aggregation under the influence of the van der Waals attractive forces. The value of the critical coagulation concentration (CCC), which marks the onset of the unstable colloidal system, corresponds to an ionic strength of 130 mM, which is close in value to the CCCs of lattices reported earlier for monovalent salt solutions.[42–45]

3.2. Functionalization of the AL with PFS(−)

The surface of AL was modified by adsorbing oppositely charged PFS(−). The effect of the PFS(−) dose on the colloidal stability was determined by measuring aggregation rates and zeta potentials in a series of AL-PFS(−) dispersions with a gradually increasing PFS(−) concentration. The main goal was to obtain negatively charged particles forming stable dispersions. The zeta potential and stability ratio data are shown in Fig. 2.

At low PFS(−) doses, AL particles are highly charged, and thus, aggregation is prevented. Increasing the polyelectrolyte concentration leads to a decrease in the zeta potential. At a dose of approximately 200 mg g^{-1}, the negative charge of PFS (−) balances the opposite charge of AL upon adsorption, *i.e.*, the particles possess an overall charge of zero, which leads to rapid aggregation due to the lack of electrical double-layer repulsion and the dominance of van der Waals forces. Applying larger doses resulted in charge reversal and thus the particles became negatively charged. At a dose of 1000 mg g^{-1}, the zeta potential values reached a steady state at the onset of the adsorption saturation plateau (ASP), at which the AL surfaces became saturated with PFS(−) chains. The dose at the ASP onset represents an optimal condition, *i.e.*, AL possesses a high magnitude of surface charge, which results in very slow aggregation. Therefore, a PFS(−) dose of 800 mg g^{-1} (denoted as p-AL particles) was selected for further measurements.

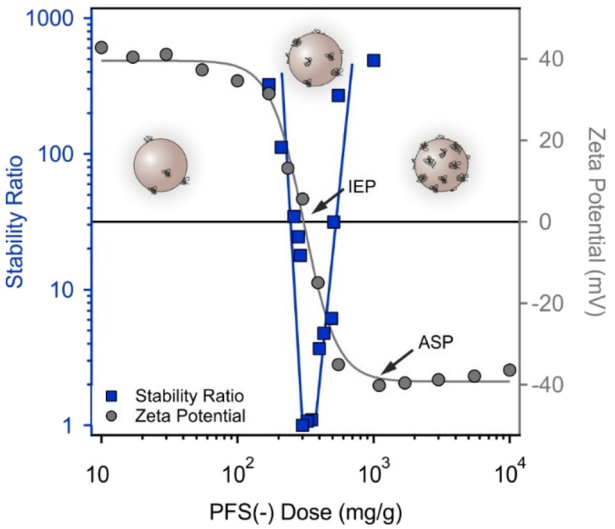

Fig. 2 Adsorption of PFS(−) on the AL at pH 4.0 and an ionic strength of 1.0 mM. Zeta potential and stability ratio of AL (25 mg L^{-1}) at different PFS(−) doses (mg PFS(−) per g AL). The solid lines serve as eye guides and the graphic insets demonstrate the increased adsorption of PFS(−) at higher doses.

Based on the data reported earlier for charged polymer–particle systems,[17–19,46,47] non-DLVO-type forces may play a role in the colloidal stability including repulsive steric as well as attractive bridging and patch-charge interparticle forces. Nevertheless, the data shown in Fig. 2 do not underline the presence of such forces unambiguously, but rather point to the domination of DLVO-type interactions.

3.3. Charge and aggregation in p-AL colloids: the effect of pH and salt

To probe the effect of the PFS(−) polymer surface layer on the stability of AL, the pH-dependent surface charge was probed at the PFS(−) dose of 800 mg g^{-1} (p-AL). Data in Fig. 3a show that the pH had no significant influence on the zeta potentials and the corresponding charge of the functionalized AL. The zeta potential was maintained at −(37.0 ± 0.6) mV throughout the pH range of 3–11 due to the presence of sulfonate groups (Scheme 2), which are deprotonated and thus provide a constant negative charge in this pH regime. The average hydrodynamic radius of the p-AL was 71.2 ± 0.2 nm under these conditions. Similar measurements with AL indicated that the mean hydrodynamic radius of bare AL was 36.6 ± 0.3 nm (Fig. 1a). The increase in size can be attributed to the two interfacial phenomena. First, the adsorbed PFS(−) polymeric

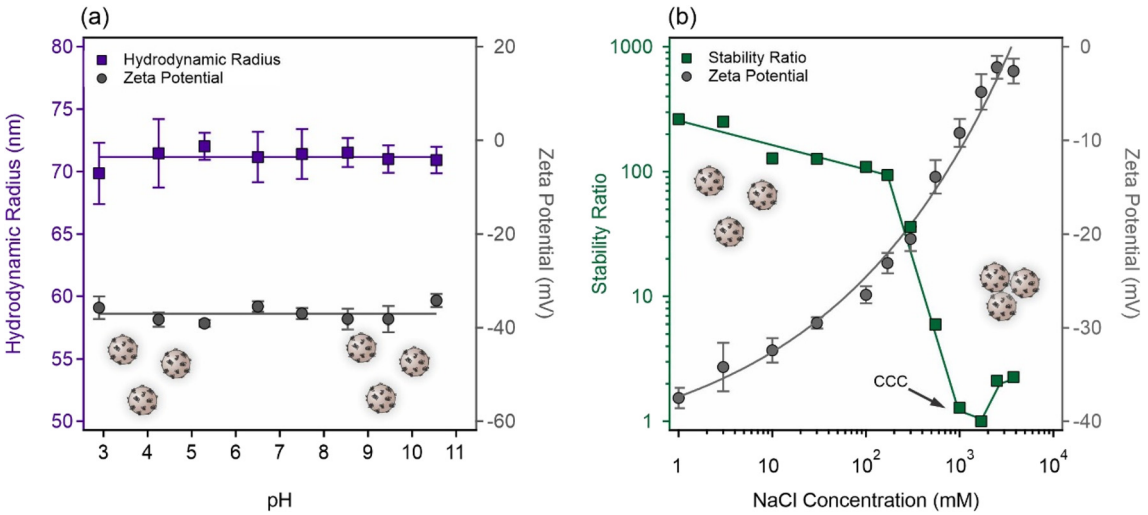

Fig. 3 Characterization of PFS(−)-functionalized AL (p-AL) at a PFS(−) dose of 800 mg PFS(−) per g AL. (a) The dependence of the hydrodynamic radius and zeta potential data for p-AL on the dispersion pH. The ionic strength was set at 1.0 mM, and the concentration of p-AL was 25 mg L^{-1}. The lines are linear fits to average the radius and potential values. (b) Zeta potential and stability ratio data of the p-AL at different ionic strengths and pH 4.0. The lines are traced for eye-guidance purposes only, while the inset graphics illustrate the aggregation status under the located conditions.

chains extending into the bulk around AL led to an increase in the hydrodynamic sphere and thus the observed hydrodynamic radius of the particles becomes larger. Second, during the adsorption of PFS(−), the process goes through a transient stage at the charge neutralization point for a very short period of time, during which the aggregation of some particles takes place, giving rise to an increase in the hydrodynamic radius of the p-AL compared to the bare counterpart.[48] However, one cannot distinguish between these scenarios based on the available experimental data.

In addition, the effect of the salt level on the colloidal stability of the p-AL was assessed in the ionic strength range of 1–3000 mM. As shown in Fig. 3b, the increased NaCl concentration resulted in a gradual screening of the surface charge, and thus, a slow decrease in the magnitude of zeta potential was observed and it reached zero around 3000 mM NaCl concentration. The trend in the stability ratios was in line with the surface charge features. Accordingly, at low salt levels (less than 100 mM), where the p-AL still maintained high zeta potential values, only slight changes were observed in the stability ratio values, indicating the absence of significant aggregation. Increasing the salt concentration led to increases in the aggregation rates because of surface charge screening.

The CCC is located around 1000 mM NaCl, which is almost one order of magnitude higher than that determined for bare AL earlier (Fig. 1b). This indicates that the presence of the PFS (−) layer on the particles improved the colloidal stability significantly. Such a high CCC was rarely reported in similar polymer–particle systems and is a sign of the presence of non-DLVO forces including steric repulsion between overlapping adsorbed polymer chains upon the approach of particles.[13–15] Similar steric stabilization was also reported for gold particles with PFS(−) layers on their surfaces.[3]

3.4. Interaction of AA with the p-AL

It was shown earlier that the redox properties of surface-bound PFS polymers change upon the addition of redox-active molecules such as AA.[3] It can be suspected that a change in the oxidation number of iron may lead to a different conformation, and hence, to a modified interfacial structure giving rise to altered zeta potentials and hydrodynamic radii. Therefore, these parameters were determined for the p-AL in the presence of AA of various concentrations (Fig. 4).

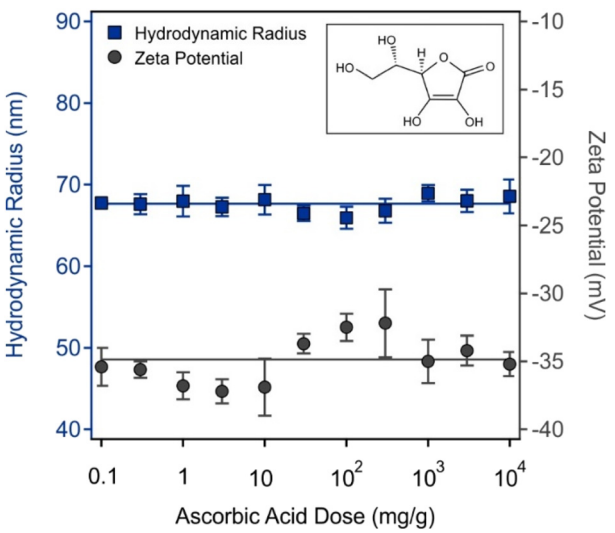

Fig. 4 Hydrodynamic radius and zeta potential data of p-AL at different doses of AA (mg AA per g AL). The structure of AA is shown in the inset. The AL concentration is 25 mg L^{-1}, whereas the pH and ionic strength are fixed at 4.0 and 1.0 mM, respectively. The solid lines are linear fits to determine the mean values.

The presence of AA had no effect on either property since the obtained values correspond to those determined for the p-AL under identical experimental conditions in Fig. 3a. For the hydrodynamic radius, an average value of (67.6 ± 0.3) nm was calculated in the AA concentration range studied, which is like the one determined for p-AL, namely (71.2 ± 0.2) nm. Given the precision of ±5 mV in the zeta potential measurements, the AA dose-dependent values can be considered the same within experimental error, yielding an average zeta potential of −(34.9 ± 0.5) mV. Therefore, it is likely that no redox reaction occurred between PFS(−) and AA due to the very similar potential of −(37.0 ± 0.6) mV determined for the p-AL. On the other hand, AA possesses no charge under these acidic conditions, so its adsorption on the p-AL does not lead to a significant change in the zeta potential. Possible immobilization of AA likely took place *via* hydrogen bonding between the hydroxyl groups of the AA and the azide functional group on the PFS(−) or amidine groups located on the p-AL surface. The interaction between AA and the particles was further investigated by the DPPH radical scavenging assay, as discussed below.

3.5. The DPPH decomposition potential

As described in the Experimental part, the radical decomposing abilities of the materials obtained were probed by DPPH assays based on the spectrophotometric detection of DPPH concentration.[35] This test is widely used to assess the antioxidant potential of materials including nanozymes.[49–51] The DPPH levels after 10 minutes of the reaction at different scavenger concentrations are shown in Fig. 5.

Initially, the individual DPPH scavenging activities of AA and PFS(−) were separately determined (Fig. 5a and b, respectively). AA is a strong antioxidant and exhibited a remarkable DPPH reduction potential with an obtained EC_{50} value of 5.13 mg L^{-1}. Free PFS(−) also showed antioxidant activity; however, a one order of magnitude higher EC_{50} value of 57.8 mg L^{-1} was determined. When mixed in a homogeneous solution, the combination of both PFS(−) and AA resulted in a much stronger reduction potential (Fig. 5c) than the individual antioxidants with an EC_{50} value of 0.25 mg L^{-1}. In this case, the AA was fixed at 5.0 mg L^{-1}, while the concentration of PFS (−) was altered between 0 and 150 mg L^{-1}. At a low PFS(−) concentration, the AA/PFS(−) curve resembles that of pure AA, while at a high PFS(−) concentration, it becomes similar to that for free PFS(−).

Fig. 6 shows the EC_{50} values and the final DPPH% for the different combinations. The numerical labels show the concentration of the antioxidant at which the maximum radical scavenging was observed. The immobilization of PFS(−) on AL resulted in a deterioration of the DPPH reduction potential (Fig. 5d) at a low PFS(−) concentration until a threshold PFS(−)

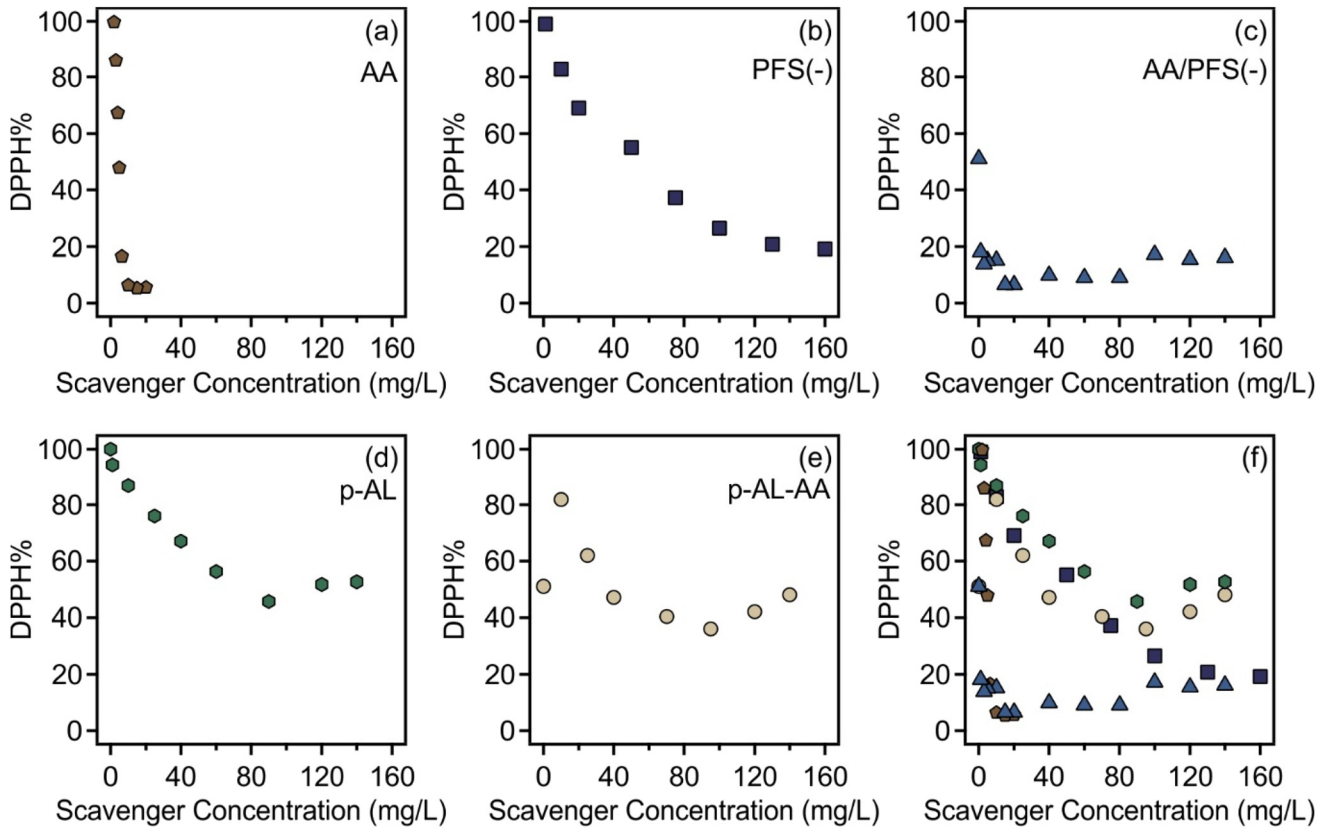

Fig. 5 The DPPH activity of (a) AA and (b) free PFS(−), (c) AA/PFS(−), (d) p-AL NPs, and (e) p-AL-AA. For comparative purposes, the activities are collected in (f). The scavenger concentration refers to the PFS(−) in all the systems, except for the bare AA, where it is equal to the AA mass concentration.

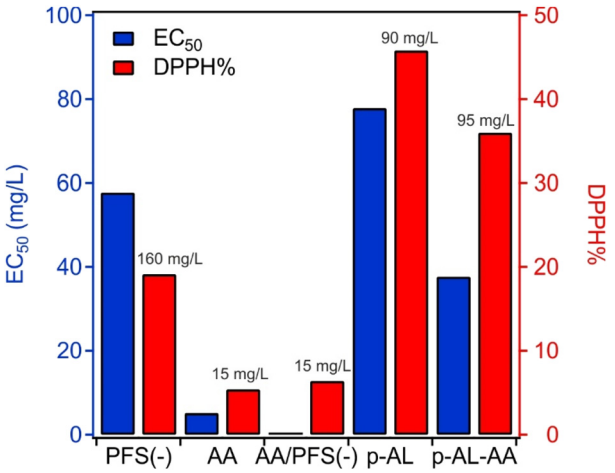

Fig. 6 Effective concentration (EC_{50}) and final remaining DPPH% data for the radical scavenger materials studied. The inset numbers indicate the scavenger concentrations, at which the maximum DPPH decompositions were observed.

concentration of 90.0 mg L^{-1} was reached, after which a weaker activity was observed with increasing scavenger loading. Nevertheless, the p-AL particles show clear antioxidant features, *i.e.*, they can be considered as an antioxidant nanozyme. The EC_{50} value of the p-AL was 77.9 mg L^{-1}. A similar trend was observed with p-AL-AA (Fig. 5e), where the AA concentration was fixed at 5.0 mg L^{-1} and the PFS(−) level was changed. At a low PFS(−) concentration, the p-AL-AA data were similar to the ones measured for free PFS(−) with a slight increase in the activity owing to the additional presence of AA. However, when the PFS(−) loading was high (above 95.0 mg L^{-1}), a deterioration in the activity was observed like in the p-AL system. Importantly, the EC_{50} value for p-AL-AA is 37.7 mg L^{-1}, which indicates a factor of two higher antioxidant activity than that for p-AL. Therefore, AL-based nanoparticles are promising antioxidant nanozymes with tuneable colloidal properties.

4. Conclusions

A thorough investigation of the colloidal and radical scavenging properties of the p-AL nanozyme system is presented. At optimal pH and ionic strength, the adsorption of negatively charged PFS(−) onto the oppositely charged latex nanoparticles took place and resulted in charge neutralization followed by charge reversal, as the PFS(−) dose was increased. A significant electrostatic repulsion was observed at high and low PFS(−) concentration values, while van der Waals forces dominated around the charge neutralization point. The obtained p-AL composite, *i.e.*, AL particles with a PFS(−) layer on the surface, exhibited excellent stability against salt-induced aggregation, as evidenced by the remarkable increase in the CCC. The addition of AA to the p-AL dispersions did not change the charge and size of the particles and thus no evidence was found either for the redox reaction between PFS(−) and AA or for AA adsorption on the p-AL. The results of DPPH assays showed that PFS(−) and AA exhibited antioxidant potential in both bare and immobilized forms and the combination of these reductants showed enhanced antioxidant potential compared to the performance of the individual components in solution. On the other hand, immobilization gave rise to deterioration of the radical decomposing performance of PFS(−), but the combination of p-AL with AA resulted in enhanced activity. This study shows the dual function of the PFS(−) polymer, namely as a stabilizer and as a basis of the antioxidant material. In addition, the rigorous stability of the p-AL nanozyme system against pH and ionic strength, as well as the preservation of antioxidant effect upon immobilization, demonstrate significant potential as a radical scavenger in applications especially in heterogeneous systems, where both colloidal stability and antioxidant activity can be important requirements.

Author contributions

NBA developed the experimental design, and performed and analyzed the DLS and antioxidant assay experiments with the supervision of IS. TH synthesized and characterized the polymer with the help of MAH. CN and JGV joint-supervised TH. NBA and IS wrote the manuscript through the contributions of TH, MAH, CN and JGV. IS and CN conceived the idea and secured financial support.

Conflicts of interest

There are no conflicts to declare.

Acknowledgements

This project received funding from the European Union's Horizon Europe research and innovation programme under the Marie Skłodowska-Curie grant agreement no. 101086226 (IS), from the Hungarian National, Research, Development and Innovation Office (TKP2021-NVA-19 and SNN142258) (IS), from the French National Centre for Scientific Research (International Emerging Action ASIDE) (CN) and from the University of Twente (MAH and JGV). Support from the University of Szeged Open Access Fund (6345) is gratefully appreciated.

References

1 J. Y. You, I. Manners and H. J. Dou, *Langmuir*, 2021, **37**, 9089–9097.
2 T. Halmagyi, J. M. Hao, M. A. Hempenius and G. J. Vancso, *ACS Appl. Nano Mater.*, 2022, **5**, 8868–8874.

3 J. Song, Y. N. Tan, D. Janczewski, M. A. Hempenius, J. W. Xu, H. R. Tan and G. J. Vancso, *Nanoscale*, 2017, **9**, 19255–19262.
4 K. Cui, Y. H. Song and L. Wang, *Electrochem. Commun.*, 2008, **10**, 1712–1715.
5 X. F. Sui, X. L. Feng, J. Song, M. A. Hempenius and G. J. Vancso, *J. Mater. Chem.*, 2012, **22**, 11261–11267.
6 G. Trefalt, I. Szilagyi and M. Borkovec, *J. Colloid Interface Sci.*, 2013, **406**, 111–120.
7 F. J. M. Ruiz-Cabello, T. Oncsik, M. A. Rodriguez-Valverde, P. Maroni and M. Cabrerizo-Vilchez, *Langmuir*, 2016, **32**, 11918–11927.
8 Y. J. Diao, M. W. Han, J. A. Lopez-Berganza, L. Valentino, B. Marinas and R. M. Espinosa-Marzal, *Langmuir*, 2017, **33**, 8982–8992.
9 I. Popa, G. Papastavrou and M. Borkovec, *Phys. Chem. Chem. Phys.*, 2010, **12**, 4863–4871.
10 Y. K. Leong, *Colloid Polym. Sci.*, 1999, **277**, 299–305.
11 D. W. Wang, B. Tejerina, I. Lagzi, B. Kowalczyk and B. A. Grzybowski, *ACS Nano*, 2011, **5**, 530–536.
12 R. J. B. Motta, A. Z. F. Almeida, B. L. B. de Lima, R. Schneider, R. D. Balaban, J. S. van Duijneveldt and R. J. de Oliveira, *Phys. Chem. Chem. Phys.*, 2020, **22**, 15–19.
13 M. B. Einarson and J. C. Berg, *J. Colloid Interface Sci.*, 1993, **155**, 165–172.
14 G. Fritz, V. Schadler, N. Willenbacher and N. J. Wagner, *Langmuir*, 2002, **18**, 6381–6390.
15 H. Huang and E. Ruckenstein, *Langmuir*, 2006, **22**, 4541–4546.
16 P. Rouster, M. Dondelinger, M. Galleni, B. Nysten, A. M. Jonas and K. Glinel, *Colloids Surf., B*, 2019, **178**, 508–514.
17 F. Iselau, T. P. Xuan, G. Trefalt, A. Matic, K. Holmberg and R. Bordes, *Soft Matter*, 2016, **12**, 9509–9519.
18 C. Vasti, A. Borgiallo, C. E. Giacomelli and R. Rojas, *Colloids Surf., A*, 2017, **533**, 316–322.
19 L. Vasarhelyi, T. Hegedus, S. Saringer, G. Ballai, I. Szilagyi and Z. Konya, *Langmuir*, 2021, **37**, 5399–5407.
20 A. Tiraferri and M. Borkovec, *Sci. Total Environ.*, 2015, **535**, 131–140.
21 L. Y. Wang, B. H. Zhu, Y. T. Deng, T. T. Li, Q. Y. Tian, Z. G. Yuan, L. Ma, C. Cheng, Q. Y. Guo and L. Qiu, *Adv. Funct. Mater.*, 2021, **31**, 2101804.
22 A. Larranaga, I. L. M. Isa, V. Patil, S. Thamboo, M. Lomora, M. A. Fernandez-Yague, J. R. Sarasua, C. G. Palivan and A. Pandit, *Acta Biomater.*, 2018, **67**, 21–31.
23 L. F. Wang, Y. Li, L. Zhao, Z. J. Qi, J. Y. Gou, S. Zhang and J. Z. Zhang, *Nanoscale*, 2020, **12**, 19516–19535.
24 S. Saringer, P. Rouster and I. Szilagyi, *J. Colloid Interface Sci.*, 2021, **590**, 28–37.
25 M. Pavlovic, M. Nafradi, P. Rouster, S. Murath and I. Szilagyi, *J. Colloid Interface Sci.*, 2019, **543**, 174–182.
26 M. Duy, M. Matrat, A. Ben Amara, F. Foucher, B. Moreau, Y. Yu, M. Goussougli, R. Fournet, B. Sirjean and P. A. Glaude, *Fuel Process. Technol.*, 2022, **236**, 107414.
27 L. Soulere and J. Bernard, *Bioorg. Med. Chem. Lett.*, 2009, **19**, 1173–1176.
28 A. V. Delgado, E. Gonzalez-Caballero, R. J. Hunter, L. K. Koopal and J. Lyklema, *Pure Appl. Chem.*, 2005, **77**, 1753–1805.
29 P. A. Hassan, S. Rana and G. Verma, *Langmuir*, 2015, **31**, 3–12.
30 C. Glaubitz, B. Rothen-Rutishauser, M. Lattuada, S. Balog and A. Petri-Fink, *Nanoscale*, 2022, **14**, 12940–12950.
31 H. Holthoff, S. U. Egelhaaf, M. Borkovec, P. Schurtenberger and H. Sticher, *Langmuir*, 1996, **12**, 5541–5549.
32 C. Takeshita, K. Masuda and M. Kobayashi, *Colloids Surf., A*, 2019, **577**, 103–109.
33 A. Baschieri and R. Amorati, *Antioxidants*, 2021, **10**, 1551.
34 C. Liu, Y. Y. Yan, X. W. Zhang, Y. Y. Mao, X. Q. Ren, C. Y. Hu, W. W. He and J. J. Yin, *Nanoscale*, 2020, **12**, 3068–3075.
35 W. Brand-Williams, M. E. Cuvelier and C. Berset, *Lebensm. Wiss. Technol.*, 1995, **28**, 25–30.
36 A. M. Smith, P. Maroni and M. Borkovec, *Phys. Chem. Chem. Phys.*, 2018, **20**, 158–164.
37 T. C. Cao, M. Borkovec and G. Trefalt, *Colloids Interfaces*, 2020, **4**, 52.
38 N. B. Alsharif, K. Bere, S. Sáringer, G. F. Samu, D. Takács, V. Hornok and I. Szilagyi, *J. Mater. Chem. B*, 2021, **9**, 4929–4940.
39 A. Hakim, M. Nishiya and M. Kobayashi, *Colloid Polym. Sci.*, 2016, **294**, 1671–1678.
40 T. Sugimoto, M. Nishiya and M. Kobayashi, *Colloid Polym. Sci.*, 2017, **295**, 2405–2411.
41 S. H. Xu and Z. W. Sun, *Soft Matter*, 2011, **7**, 11298–11308.
42 K. Omija, A. Hakim, K. Masuda, A. Yamaguchi and M. Kobayashi, *Colloids Surf., A*, 2021, **619**, 126552.
43 T. Oncsik, G. Trefalt, M. Borkovec and I. Szilagyi, *Langmuir*, 2015, **31**, 3799–3807.
44 L. Ehrl, Z. Jia, H. Wu, M. Lattuada, M. Soos and M. Morbidelli, *Langmuir*, 2009, **25**, 2696–2702.
45 J. L. Trompette and J. F. Lahitte, *J. Phys. Chem. B*, 2019, **123**, 3859–3865.
46 A. Hajdu, M. Szekeres, I. Y. Toth, R. A. Bauer, J. Mihaly, I. Zupko and E. Tombacz, *Colloids Surf., B*, 2012, **94**, 242–249.
47 L. L. Feng and Y. Adachi, *Colloids Surf., A*, 2014, **454**, 128–134.
48 J. Hierrezuelo, I. Szilagyi, A. Vaccaro and M. Borkovec, *Macromolecules*, 2010, **43**, 9108–9116.
49 F. Moccia, D. Liberti, S. Giovando, C. Caddeo, D. M. Monti, L. Panzella and A. Napolitano, *Antioxidants*, 2022, **11**, 1681.
50 J. Matysik, J. Loureiro, M. D. D. Pereira, M. Banach and O. Dfugosz, *J. Mater. Sci.*, 2022, **57**, 15954–15966.
51 Y. Y. Mao, F. M. Jia, T. Y. Jing, T. T. Li, H. M. Jia and W. W. He, *ACS Sustainable Chem. Eng.*, 2021, **9**, 569–579.